

Ultrathin Eardrum-Inspired Self-Powered Acoustic Sensor for Vocal Synchronization Recognition with the Assistance of Machine Learning

Yang Jiang, Yufei Zhang, Chuan Ning, Qingqing Ji, Xiao Peng, Kai Dong,*
and Zhong Lin Wang*

With the rapid development of human–machine interfaces, artificial acoustic sensors play an important role in the hearing impaired. Here, an ultrathin eardrum-like triboelectric acoustic sensor (ETAS) is presented consisting of silver-coated nanofibers, whose thickness is only 40 μm . The sensitivity and frequency response range of the ETAS are closely related to the geometric parameters. The ETAS endows a high sensitivity of 228.5 mV Pa^{-1} at 95 dB, and the ETAS has a broad frequency response ranging from 20 to 5000 Hz, which can be tuned by adjusting the thickness, size, or shape of the sensor. Cooperating with artificial intelligence (AI) algorithms, the ETAS can achieve real-time voice conversion with a high identification accuracy of 92.64%. Under good working property and the AI system, the ETAS simplifies signal processing and reduces the power consumption. This work presents a strategy for self-power auditory systems, which can greatly accelerate the miniaturization of self-powered systems used in wearable electronics, augmented reality, virtual reality, and control hubs for automation.

1. Introduction

Hearing loss is a widely prevalent disability of all ages and growing constantly, especially for adolescents and the elderly, which is partly caused by the damage of the eardrum. Hearing aids with acoustic sensors have attracted extensive attentions to provide eardrum services for hearing-impaired people, including dynamic, capacitor, electret condenser, or piezoelectric microphone, etc.^[1–7] Nevertheless, these acoustic sensors often lack aesthetics and comfortability for long-term wearing. And they must rely on external batteries, which need frequently charged. In addition, various wearable electronics combined with artificial intelligence (AI) and Internet of Things (IoTs) technology are receiving intensive attentions to provide better human–machine interaction (HMI) devices.^[8–11] Among them, acoustic

sensors integrating with AI algorithms are of paramount significance for hearing-impaired people. Future acoustic sensors are required to detect the analog sound wave, which can convert it into digital signals to store the information and analyze synchronously. However, frequent and deep HMI have to generate immense information, which cannot be supported by traditional power sources owing to its limited capacity. Hence, one of the most promising alternatives to address such issues is to develop self-powered acoustic sensors with higher sensitivity, broader frequency response, and smaller size. There are many self-powered acoustic sensors based on the piezoelectric effect, which unitizes the micro-electro-mechanical system.^[12–15] However, commercial application of these piezoelectric acoustic sensors is restricted by their low electric output, complicated structure, and improper frequency range of voice recognition.

Fortunately, triboelectric nanogenerator (TENG) is the application of Maxwell's displacement current, which is first invented by Wang and co-workers in 2012.^[16–18] TENG has been considered as an energy harvesting technology for the new era, and intensive advancements of them have been achieved in micro-/nanopower sources,^[19–22] self-powered sensors,^[23–28] high-voltage sources,^[29–32] and blue energy harvesting.^[33–35] Based on the coupling of triboelectrification

Y. Jiang, Y. Zhang, C. Ning, X. Peng, K. Dong, Z. L. Wang
Beijing Institute of Nanoenergy and Nanosystems
Chinese Academy of Sciences
Beijing 101400, P. R. China
E-mail: dongkai@binn.cas.cn; zlwang@gatech.edu

Y. Jiang, Y. Zhang, C. Ning, X. Peng, K. Dong, Z. L. Wang
School of Nanoscience and Technology
University of Chinese Academy of Sciences
Beijing 100049, P. R. China

Q. Ji
Institute of Computing Technology
Chinese Academy of Sciences
University of Chinese Academy of Sciences
Beijing 100049, P. R. China

Z. L. Wang
CUSTech Institute of Technology
Wenzhou, Zhejiang 325024, P. R. China

Z. L. Wang
School of Materials Science and Engineering
Georgia Institute of Technology
Atlanta, GA 30332-0245, USA

 The ORCID identification number(s) for the author(s) of this article can be found under <https://doi.org/10.1002/sml.202106960>.

DOI: 10.1002/sml.202106960

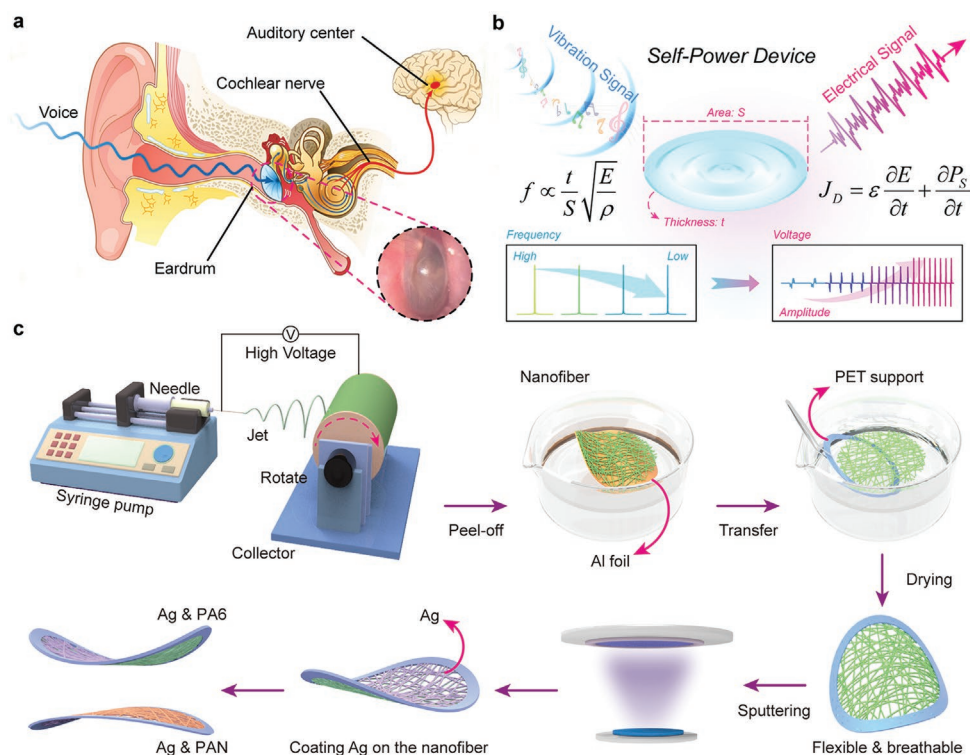


Figure 1. The overall concept of all-nanofiber eardrum-like, an ultra-thin acoustic sensor (ETAS). a) Schematic illustration of the overall concept of biomimetic and miniaturized the ETAS. b) Illustration of biomimetic ultrathin film mimicking the eardrum-like membrane of the human cochlea for converting analog sound waves into electrical signals. c) The fabrication process of the ETAS consisting of PAN and Ag and PA6 and Ag nanofibers.

and electrostatic induction, TENG has several advantages, including high electric output, microscale motion detection, and weak physiological signals monitoring from the human body. Recently, researchers find that TENGs also possess a huge potential in harvesting the microvibration energies, such as acoustic waves, which exist ubiquitous but are regrettably ignored.^[13,36–40] Triboelectric acoustic sensors have the advantages of high sensitivity, self-powered operation, and proper frequency response for the sound spectrum, indicating that it is an effective strategy to prepare the artificial cochlear implantation.^[41,42] However, there are few researches of the triboelectric acoustic sensor using organic film with designed holes or microstructure on its surface, such as the polytetrafluoroethylene (PTFE)/copper thin film with a holey aluminum film, PTFE/copper film with a holey paper/copper film, and Kapton/Au film with holey fluorinated ethylene propylene (FEP)/Au film.^[43–45] These TENGs can collect acoustic signals based on the contact–separation mode. Furthermore, they rely on a Helmholtz cavity or complex surface treatment process, which means that they are often fabricated on rigid, thick and air impermeable substrates. And it will induce inflammation after a long time of wearing. Notably, it is a huge challenge to achieve the high sensitivity and downsizing acoustic sensor simultaneously, because the sensitivity and resonant frequency are reduced with the dimension size diminution. Moreover, these acoustic sensors lack the deep HMI, such as the perceiving and transforming the human voice, which is desperately eager for the hearing-impaired.

Herein, we report a universal and convenient method to prepare an ultrathin eardrum-like triboelectric acoustic sensor (ETAS) consisting of all flexible nanofibers. Inspired by the eardrum, a multi-hole elastic nanofiber film is fabricated by electrospinning, and ETAS consists of the two films which are prepared by coating silver (Ag) on the polyacrylonitrile (PAN) and polyamide 6 (PA6) nanofiber by magnetron sputtering, respectively. The ETAS has a 40 μm thickness and ultrahigh sensitivity up to 228.5 mV Pa⁻¹ at 95 dB. Furthermore, the ETAS has a broad frequency response (20–5000 Hz), and tunable frequency response by adjusting the size and shape of the sensor. With the optimized AI algorithm, the ETAS can achieve high identification accuracy. To satisfy the practical application, the ETAS is combined with the optimized AI algorithm to achieve real-time voice conversion, which can obtain a high identification accuracy of 92.64%. We predict that this ETAS exhibits a prospective application in accurate voice recognition, high-performance self-powered acoustic, or robotic artificial intelligence.

2. Result and Discussion

2.1. Overall Concept of ETAS

The biomimetic eardrum-like acoustic sensor is fabricated by imitating the tympanic membrane of the human. **Figure 1a** shows a schematic illustration of the overall concept of biomimetic and miniaturized ETAS. Located at the bottom of the external auditory canal, the eardrum is the oval, light gray, and translucent

film, which is considered as the link between the external and the middle ear. Figure 1b schematically illustrates the frequency spectral variation and mobile voice perception of miniaturized ETAS. The ultrathin nanofiber possesses a thickness of 40 μm , which can be used for converting sound vibration to electrical signals. The ETAS endows tunable resonance frequency f which can be adjusted by modifying the geometric parameters of the device. And the specific relationship can refer to the Equation 1

$$f \propto \frac{t}{S} \sqrt{\frac{E}{\rho}} \quad (1)$$

where f is the resonance frequency, S and t are the area and thickness of the ETAS, respectively. E and ρ are the elastic modulus and density of the nanofiber film, respectively.

The principle of the ETAS can be derived from the displacement current density J_D in Maxwell's equations, which was discovered by Wang and co-workers^[46,47]

$$J_D = \varepsilon \frac{\partial E}{\partial t} + \frac{\partial P_s}{\partial t} \quad (2)$$

where ε , E , P represents the permittivity of the material (or medium), the electric field, and the polarization of the dielectric material, respectively. The procedure to fabricate ETAS is shown in Figure 1c. First, the nanofiber membranes are prepared by electrospinning: (1) polymer solution is injected into a syringe with a metal needle; (2) solution is ejected from the needle with the high voltage; (3) the polymer nanofiber is collected by rotated collector coated with aluminum foil. Second, the nanofiber membranes are transformed by using the water transferred method. Third, PET support is placed under nanofiber to obtain a flat and smooth film. Then, drying up the film which can make it tighten, and the flexible, tighten, and permeable nanofiber film can be obtained. The film is followed by depositing the Ag layer on its surface via the magnetron sputtering. Finally, PAN and PA6 coated with Ag are assembled together to form the acoustic sensor due to the large difference in electronegativity. The above method is a general strategy to prepare various flexible conductive films, and poly urethane (PU), thermoplastic urethane (TPU), polyvinyl alcohol (PVA), polyvinyl chloride (PVC), poly(vinylidene fluoride) (PVDF), and other flexible films.

2.2. Structural Design and Characterization

Figure 2a shows that the structure of the ETAS consisting of two layers, including Ag and PAN and Ag and PA6 nanofibers. In detail, the nanofibers are flexible, and thin, coated with Ag electrode by magnetron sputtering. In order to acquire the better performance of nanofiber film, the influence of electrospinning parameters on the nanofiber morphology is studied, including solution concentration, electrospinning voltage, flow rates, receiving distances, and etc. The details can be found in Figure S1 in the Supporting Information. Among those, the optimum electrospinning parameters for the PA6 is 10 wt%, 18 kV, and 0.2 mL h^{-1} , and for PAN is 20 wt%, 18 kV, and 0.3 mL h^{-1} . And the SEM image of PA6 nanofiber film under

the above parameters is shown in Figure 2b. Moreover, a cross-sectional image of PA6 nanofiber proves that Ag is uniformly deposited on its surface (inserted in Figure 2b). More detailed SEM images can refer to the supporting information (Figure S4, Supporting Information). Figure 2c shows that the average diameter of PA6 nanofiber is about 50 nm. As shown in Figure S2 (Supporting Information), the surface morphologies SEM of the PAN, Ag and PAN, PA6, and Ag and PA6 nanofiber films have no obvious difference. This demonstrates that the Ag coating is uniformly and thin. The optical photograph of the nanofiber film in Figure 2d exhibits high transparency, and the transmittance of the nanofiber film is shown in Figure S3c in the Supporting Information. Excellent air permeability increases the comfortability for wearing. Both nanofiber films (Ag and PAN or Ag and PA6) in the device exists high air permeability under different pressure due to the nanofiber structure (shown in Figure 2e). Moreover, the air permeability is increased with the pressure increase, and the air permeability of the device approximates to the air permeability of compact Ag and PA6 film. This phenomenon can be explained that the air permeability of the whole device is limited by the layer with poor air permeability. Furthermore, the silver-coated film has almost the same air permeability as the original film with the test pressure ranging from 100 to 700 Pa, indicating that the Ag on the fiber surface only affects its diameter and would not affect its permeability (Figure S3, Supporting Information). The cross-sectional images of PAN nanofibers, PA6 nanofibers are shown in Figure S4 in the Supporting Information. The element analysis of the nanofiber through energy-dispersive X-ray spectrometry (EDX) can be seen in Figure 2f, Figures S5–S8 (Supporting Information), and Ag, C, N, and O elements are evenly distributed in the nanofibers.

2.3. Working Mechanism and Output Performance

The specific working principle of the ETAS is illustrated in Figure 3a. It can harvest the energy from the vocal vibration based on the coupling of triboelectrification and electrostatic induction. The vibrational energy harvesting of the film can be simplified into four steps. The PAN film is proven to be negatively charged due to the stronger electronic attraction. When the two nanofiber films contact with each other, the opposite charges with the same amount are generated at the two contact surfaces of the film (Figure 3a-i). Notably, the polymers can maintain the triboelectric charges for a long time due to the insulating properties. Since these opposite charges distribute on almost the same plane, there are no electric potential differences and electrons flow between the two electrodes. As they start to separate from each other, different potential is generated, yielding electrons flow from the PA6 side electrode through external loading to the PAN side electrode (Figure 3a-ii). With the two films separate quite far away, a new electrical equilibrium achieves and the electrons stop moving (Figure 3a-iii). Subsequently, electron flowing is inversely from the PA6 side electrode through external loading to the PAN side electrode when the two films approach each other again (Figure 3a-iv). Charge neutralization is achieved again after the two films are fully in contact with each other, and the continuous alternating

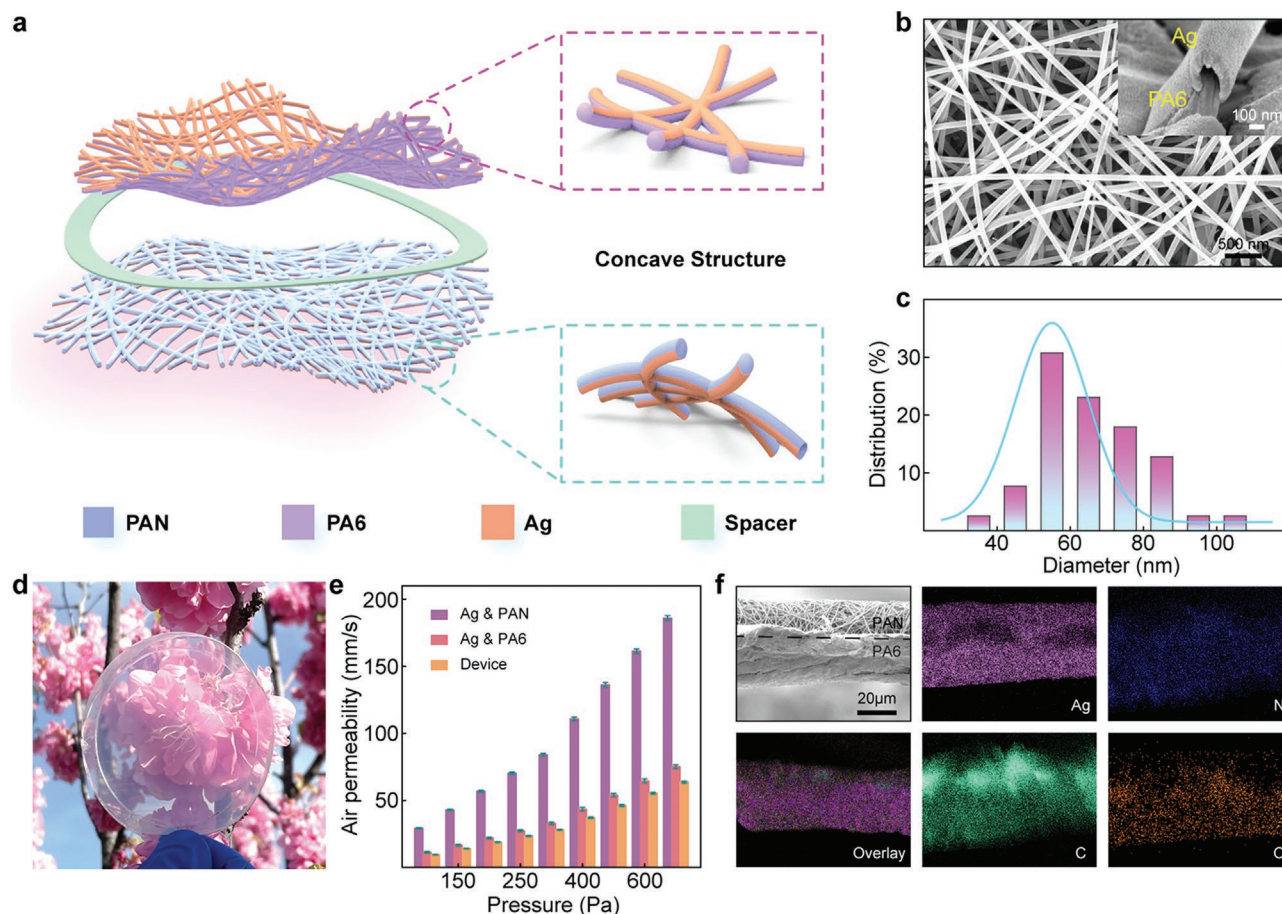


Figure 2. Structural design and characterization of the ETAS. a) Schematic illustration of the 3D network structure of the ETAS, enlarged image shows the nanofiber coated with Ag. b) Optimized surface morphology SEM images of PA6, the cross-sectional enlarged image of the Ag uniformly deposited on the PA6 nanofiber is inserted. c) The diameter distribution of PA6. d) Optical photograph images of the nanofiber film. e) The air permeability of Ag and PAN film, Ag and PA6 film, and device under different pressure. f) Surface morphology SEM images of the cross-sectional ETAS, and energy-dispersive X-ray spectrometry (EDX) elemental mappings of the ETAS.

current from ETAS can be obtained from the continuous contact–separation movements between the PAN film and the PA6 film. Further quantitative analysis of the charge generation process, a theoretical model of the ETAS is used to study the potential distribution of PAN film and PA6 film during the contact-separation movements by the finite element simulation using COMSOL (Figure 3b).

As shown in Figure 3c, the output current increases with the external frequency ranging from 0.5 to 5 Hz. The contact area is chosen as 20 cm² with the tapping force of 0.1 N, and the maximum movement distance is set as 20 mm. Furthermore, the effective output performance of the ETAS under different resistances is measured. The maximum output current of the ETAS drops with the increasing external resistances. Instantaneous power density is maximized at a load resistance of 400 MΩ, corresponding to a peak power density of 0.8 mW m⁻², as shown in Figure 3d. Moreover, the charging ability of the ETAS is measured under different capacitance capacities, and the charging speed accelerates as the reducing capacitance (Figure 3e).

As per the test conditions, the frequency of contact-separation cycle is 3 Hz under pressure of 13 Pa, and the voltage of the

capacitance is measured by the Keithley 6514. It means that the ETAS can serve as a micropower source, which can sustainably power wearable electronics. As depicted in Figure 3f, the V_{OC} , I_{SC} , and Q_{SC} of the ETAS under different pressure applied by Lin Mot E1100 are quantitatively measured, which are rising gradually as increasing pressure from 1.5 to 180 Pa. These demonstrate that ETAS has excellent properties in the low-frequency range.

In the high-frequency range, the ETAS also has good electrical properties and frequency response behaviors. The ETAS produces different electric signals of voltage, charge, and current (Figure 3g,h; Figure S9, Supporting Information) under different external frequencies, and it can be found that the output voltage is positively correlated with frequency at a certain range.

2.4. Acoustic Response Performance

The principle of the ETAS under sound vibration is shown in Figure 4a, and the voice pressure spreading to the film through

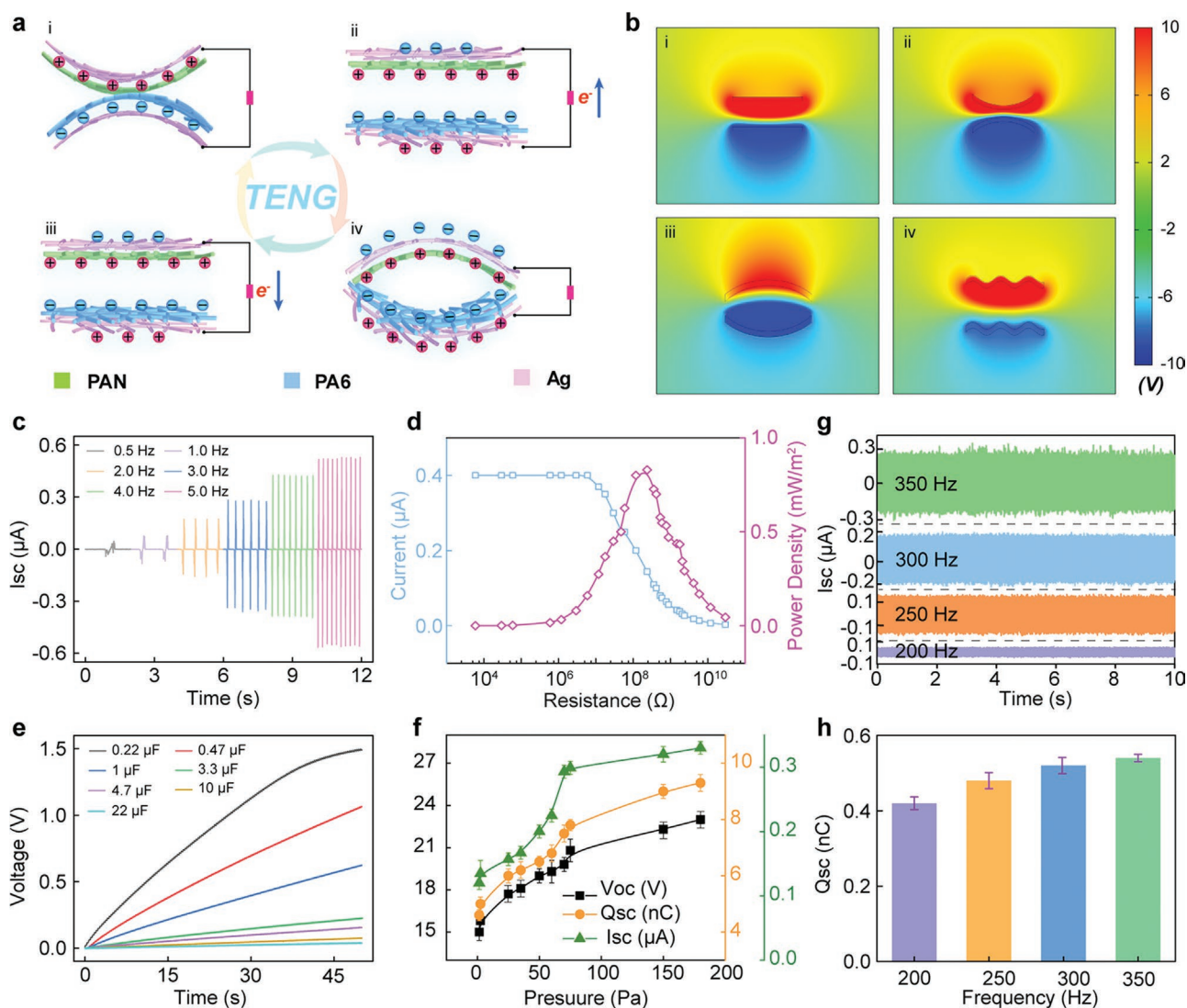


Figure 3. Working mechanisms and electric output performance. a) Schematics of the working principle for the ETAS under the vocal vibrations. b) Simulated electric field distribution of the TENG simulated by COMSOL. c) The output current of the ETAS under different frequencies (0.5–5 Hz). d) Output current and power density of the ETAS under different external load resistances and at a tapping frequency of 1 Hz. e) Charging curve of the ETAS under different capacitance capacities. f) Voltage, charge, and current of the ETAS under different pressure. Different electric output of g) current and h) charge of the ETAS under different frequencies.

the air will cause the film to stretch or shrink. It means that there is a contact–separation process between the two films, which will convert the vibration to the electrical signal based on the mechanism of the TENG. More details can refer to Figure S10 in the Supporting Information. To systematically investigate acoustic sensing performance, we fabricated the ETAS with different geometric parameters. For the axisymmetric film, the membrane vibration mode conforms to the Helmholtz and time-harmonic equation

$$T_m \frac{\partial}{\partial r} \left(r \frac{\partial u_m}{\partial r} \right) + T_m k_m^2 r u_m - i \omega r (p_m - p) = 0 \quad (3)$$

$$k_m^2 = \frac{\omega^2 \rho_{ms}}{T_m} \quad (4)$$

where T_m is the constant tension of the film, k_m is the wave of the film, r is the radial coordinates, U is the displacement of the film, P is the pressure, ρ is the polar radius and ω is the angular frequency. Deforming displacements and pressure distribution of a circular membrane with three acoustic frequencies are simulated by COMSOL Multiphysics (Figure 4b), which simulated resonant frequencies are 562.65, 884.01, 1201.1, respectively. This difference between the simulated resonant frequencies and the actual resonant frequencies can be attributed to the simplified simulated conditions and the complex vibration of nanofibers. To further investigate the film vibration, we use a high-speed camera to observe the film vibrations process induced by sound waves. Figure S11 and Movies S1–S5 (Supporting Information) depict the subtle gradations of the exciting film vibration, and it can be found that the film periodically vibrates up and down by different sonic frequencies

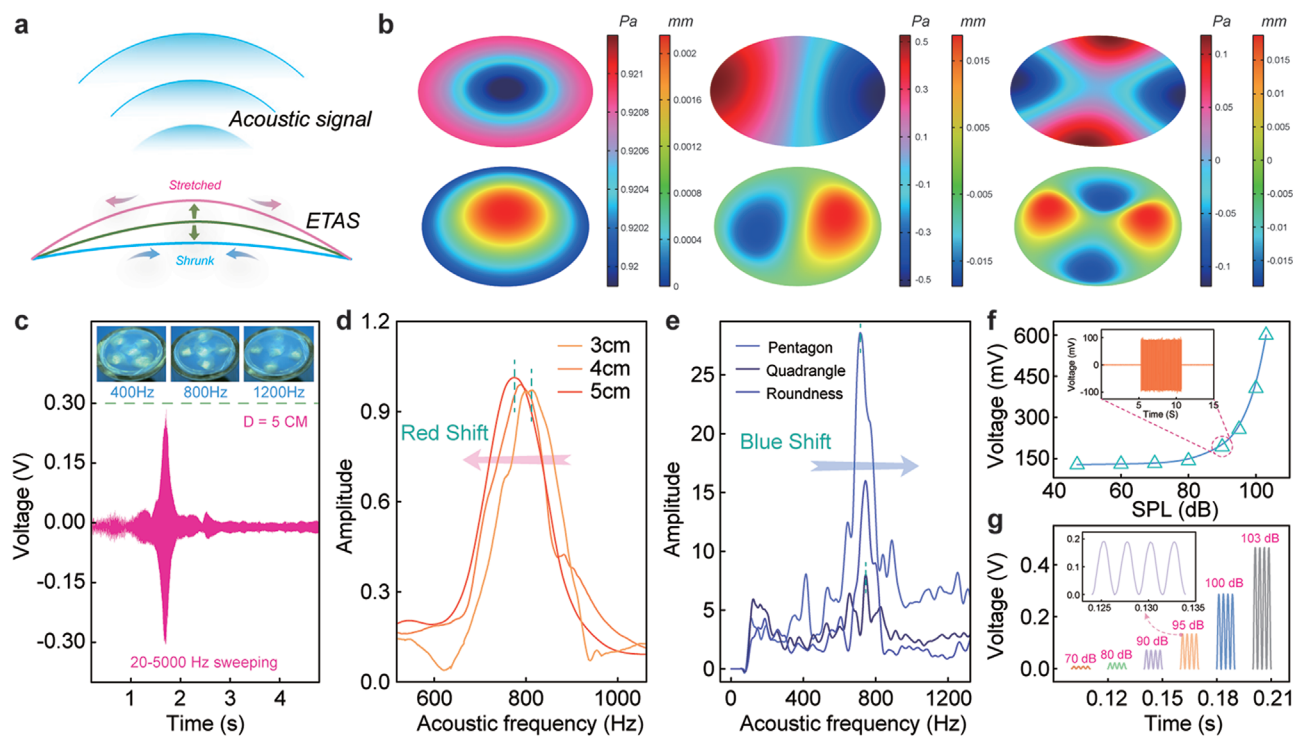


Figure 4. Characterization of acoustic response performance of the ETAS. a) Scheme of the vibration of the film. b) Deforming displacements and pressure distribution of the film under different frequencies (simulated using COMSOL under sound pressure). c) Voltage signal measured from ETAS (sweeping frequency range, 20–5000 Hz; sound intensity, 70 dB_{SPL}). The frequency spectrum of ETAS is derived through Fourier transform when varying d) size and e) shape of the device. f) The acoustic response of an ETAS ($D = 5$ cm) under various sound intensities. Inset: Acoustic response difference between the noise and specific sound signal (around 70 dB). g) A voltage signal of the ETAS under the excitation of acoustic waves with different sound pressure levels.

(400, 500, 800, 1200, 1500 Hz). Furthermore, the output signal of the ETAS is measured with a constant frequency of 200, 300, and 400 Hz. The results show that the voltage output is relatively stable with the external excitation (Figure S12a–c, Supporting Information), and whose frequency is consistent with the external frequency through Fourier transformation (Figure S12d–f, Supporting Information).

The acoustic sensor with different geometrical parameters under the external excitation has been studied to investigate its voice detection capabilities. Figure 4c shows the voltage signal under the acoustic frequency range from 20 to 5000 Hz, including the basic frequency range of communication for human beings. Digital photographs of film vibration with different frequencies are inserted in Figure 4c. It can be found that the voltage of the sensor shows different variations under the sweeping frequency measurement conditions, and the maximum value is reached at ≈ 790 Hz which may be the resonance frequency of the whole test device. In order to further study the influencing factors of resonant frequency, we fabricate ETAS with different geometric parameters, such as shapes, sizes, and thicknesses. As for the circular film, the diameter and the thickness have essential effects on the frequency response. The ETAS with different diameters (30, 40, 50 mm) and thicknesses (6.5, 8, 16.3, 38.4, 49.9 μm) are fabricated to study the resonant frequency. Under the sweeping frequency ranging from 20 to 5000 Hz at a constant speed changing in the time of 4 s, these devices of different diameter films show different voltage signals (Figure S13, Supporting Information). And the deforming

displacements of different diameter films are simulated in Figure S14 in the Supporting Information. Figure 4d shows frequency spectra of the ETAS with different membrane diameters through the Fourier transform. The results demonstrate that the ETAS with a larger diameter has a lower resonant frequency, corresponding to Equation 1. In addition, voltage signal and corresponding frequency spectra of the ETAS with different thicknesses are shown in Figures S15 and S16 in the Supporting Information. These curves indicate that the ETAS with a thicker film has a higher resonant frequency which is also consistent with Equation 1. Moreover, the sensors with different shapes, including pentagon, quadrangle, and circular devices are studied to observe the frequency response. The voltage signal and corresponding frequency spectra of the ETAS with a different shape are depicted in Figure 4e and Figure S17 (Supporting Information), and the resonant frequency has the trend of blue shift. COMSOL Multiphysics is simulated to illustrate the deforming displacements and charge distribution of different shape devices (Figure S18, Supporting Information).

The sensitivity is a paramount indicator for the high-performance acoustic sensor. The pressure of the human hearing range is relatively wide, but the sound intensity which people feel depend on the proportion of sound pressure to the absolute pressure. The sound pressure level can be measured by Equation 5

$$L_p = 10 \lg \left(\frac{p}{p_0} \right)^2 = 20 \lg \left(\frac{p}{p_0} \right) (\text{dB}) \quad (5)$$

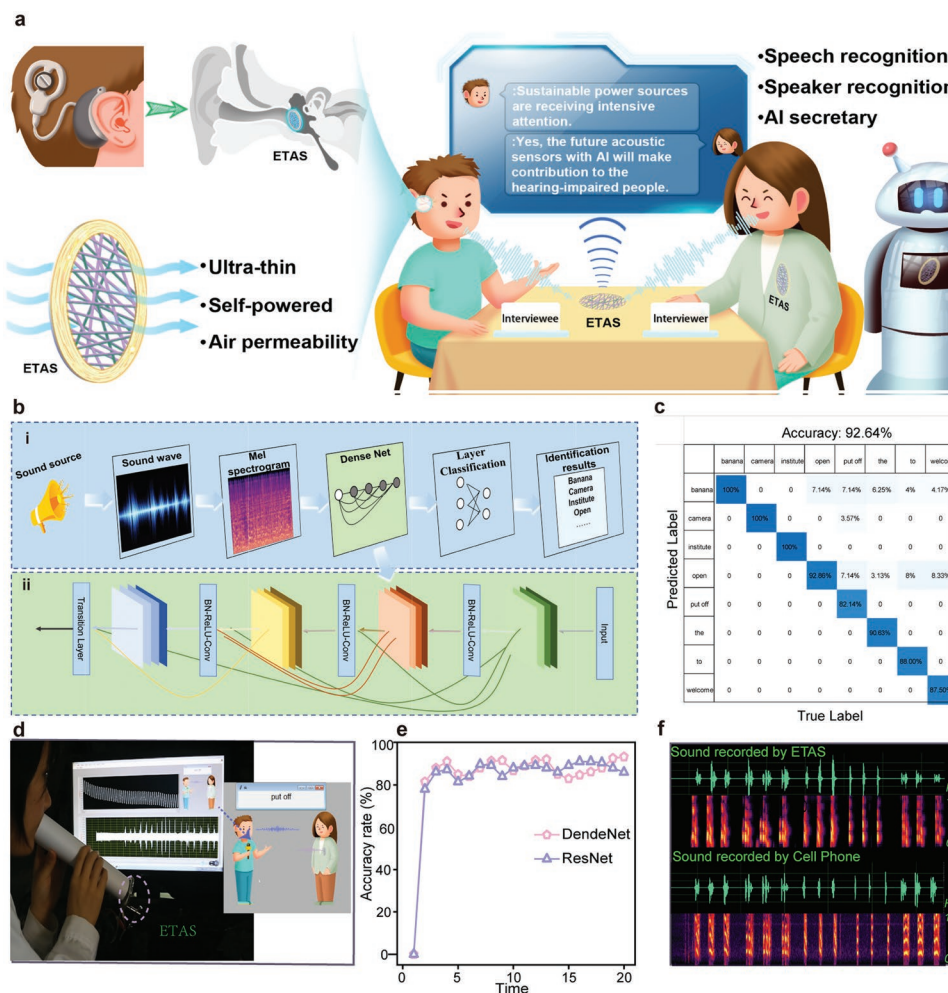


Figure 5. Application of the ETAS for voice-text conversion. a) Proposed ETAS wearable with hearing aids to allow a hearing-impaired person to interview. b) Schematic diagram of voice-to-text conversion process using the ETAS module. c) The confusion map for machine learning outcome. d) Real-time voice-to-text conversion demonstrated by the ETAS module. e) Accuracy comparison of the DenseNet and ResNet. f) Recorded sound wave information and sound spectrograms recorded by the ETAS and a cell phone.

$$S = \frac{V}{P} = \frac{V}{P_0 \cdot 10^{L_p/20}} \quad (6)$$

where S is the sensitivity, V is the root mean square value of voltage, P is the sound pressure, and P_0 is the reference sound pressure of 2×10^{-5} Pa, L_p is the sound pressure level.

Under the sound pressure level (SPL) varying from 40 to 103 dB, the voltage signal is increased with the sound intensity at a frequency of 400 Hz (Figure 4g). According to Equation 6, the sensitivity can be measured by a voltage signal. Furthermore, the ETAS achieves a sensitivity of 228.5 mV Pa^{-1} at 95 dB, and a maximum sensitivity of 715 mV Pa^{-1} with sound pressure from 80 to 103 dB (305 mV Pa^{-1} – 90 dB, 228.5 mV Pa^{-1} – 95 dB, 203 mV Pa^{-1} – 100 dB, and 212 mV Pa^{-1} – 103 dB). Furthermore, Figure S19 (Supporting Information) shows that the sensitivity decreases with dimension decreases, and Table S1 (Supporting Information) shows the comparison of the performance of self-powered acoustic sensors. Besides, ETAS has good durability for 1000 cycles under 70 Pa, shown in Figure S20 in the Supporting Information. As shown in the inset of Figure 4f,

the voltage output is significantly different from the noise. In detail, Figure 4g depicts that the output voltage is stable at a certain frequency and grows with the sound pressure from 45 to 104 dB. The voltage signal is increased from 47 to 612 mV as the sound pressure level increases from 45 to 104 dB.

2.5. Application of ETAS

Driven by global demographic trends, hearing loss is a widely prevalent disability for the whole age, especially for adolescents and the elderly. The hearing loss hinders their life and career development, for example, people suffering from hearing impairment are not competent as an interviewer. By virtue of the ETAS, the hearing loss has a chance to communicate and even interviewee with others normally. Furthermore, the excellent compatibility of the ETAS for humans promotes its development for the hearing aid. A person with hearing loss, wearing the ETAS, can interview and converse the voice into text timely (Figure 5a).

Figure 5b-i displays a flowchart of the testing procedures for the voice-text conversion, which is based on the dense convolutional network (DenseNet). The voice is converted by the ETAS, and abstracted the feature value by the Mel spectrogram. Then, the sound signal with extracted feature values is input into DenseNet to train. Finally, the classification network is used to classify and identify the real-time sound data. In detail, the dense block, as the main part of the DenseNet, is displayed in Figure 5b-ii. The dense block with a dense connection can narrow the networks, which can easily transmit the features and train voice signals. Furthermore, it has a regularization effect, inhibiting overfitting, which has better performance in the stage of model testing and prediction. Furthermore, the overall structure of DenseNet is shown in Figure S21 (Supporting Information), which contains multiple dense blocks. Every dense block is pooling the feature values and the number of the feature values shall be reduced. Due to the multiple dense blocks, the length of the voice input can be any length, which can realize real-time voice-to-text conversion. ImageNet and dataset for environmental sound classification (ESC-50) data set are used for pretraining, so that the network can capture sound features. Then, the obtained pre-training model is used for mixed training with ESC-50 data set. After 70 rounds of training, total recognition accuracy reaches 92.64%, indicating the trained model has a high positive predictive value and a true positive rate for voice recognition (Figure 5c).

By virtue of the ETAS, a speaker's voice is converted into text timely, shown in Figure 5d and Movie S6 (Supporting Information). Accurate voice biometrics is successfully demonstrated using the multi-signal characteristics of the ETAS module with these small amounts of training and testing data. Furthermore, to verify the advantages of the model in this paper, we train the voice data with DenseNet and Residual Network (ResNet) for 20 rounds of training (Figure 5e). The results verify that the model convergence tended to be relatively stable. The accuracy of the DenseNet network achieves 93.25% in the test set, while the accuracy of the ResNet network in the test set is only 86%. Figure 5f presents the collect voice signal of the waveform diagram and spectrum diagram, which is collected by the ETAS and a cell phone separately. The results demonstrate the ETAS had an excellent performance of recording and converting voice. Combined with the AI algorithm, the ETAS achieves the accurate voice-to-text conversion timely by less voice training.

2.6. Conclusion and Perspective

In summary, we have demonstrated ETAS consisting of the silver coating on the various nanofibers. The triboelectric acoustic sensor possesses high acoustic sensitivity of 228.5 mV Pa^{-1} at 95 dB and a wide frequency response ranging from 20 to 5000 Hz. Tunable frequency response can be obtained with the different geometric structure designs. Collaborated with AI algorithmic design, the ETAS can achieve speech recognition with a high identification accuracy of 92.64%, indicating promising application for HMI and benefiting hearing-impaired people. The ultrahigh and air-permeable advanced acoustic sensor provides an alternative avenue for the new AI services

such as biometric authentication and personalized IoT services in the development of robotics.

A high-performance acoustic sensor with high sensitivity and wide detection range is essential for human communication, health, and safety. However, the ETAS is still difficult to combine with the wireless transmission technology. Hence, designing a proper wireless data collection module can be considered to improve the performance of the device in future work.

3. Experimental Section

Fabrication of Nanofiber Films: The PAN (molecular weight of $\approx 80\,000$) powder was dissolved in a DMF solution at a concentration of 10 wt%. Stir the mixture at 60 °C for 6 h by magnetic stirring. Then, a homogeneous polymer solution at this concentration obtained a proper viscosity for electrospinning. The PAN solution was poured into a 5 mL plastic syringe. The electrospinning process was conducted at a positive voltage of 15 kV and a negative voltage of 2 kV. The distance between the needles and the collector distance was set to be 20 cm. The pump rates for the PAN electrospinning were set to be 0.3 mL h^{-1} . The PAN nanofiber films were collected on the aluminum foil coated on a revolving roller.

To get the PA6 solution, PA6 powder was dispersed to DMF solution at a concentration of 10 wt%, then mixed at 60 °C for 4 h by magnetic stirring. A syringe pump was used to control the flow rate of the solution (0.2 mL h^{-1}), and a constant potential (18 kV) was applied between the needle and grounded collectors to form the PA6 nanofiber film.

The nanofiber film prepared was put on the water surface, and peeled off the aluminum foil underwater. A circular ring PET film was prepared by a laser cutting machine. To obtain a flat and smooth film, the PET support was placed under nanofiber film. Finally, dry up the nanofiber films at room temperature. The PAN and PA6 nanofibers were then coated on silver with a thickness of 200 nm by magnetron sputtering for 720 s.

Characterization and Measurement: A Nano SEM 450 was used to measure the nanofiber structure and element analysis on the surface morphology of samples. The SEM images were used to estimate the fiber diameter using image processing software (ImageJ 1.50b). A step motor (Lin Mot E1100) was applied to provide the regular contact-separation movement for TENGs. An acquisition card (USB-6356) was adopted to test the open-circuit voltage, short-circuit current, and transferred charge. The software platform was constructed based on Labview, providing realizing real-time data acquisition. The air permeability was measured by using an air permeability apparatus (PARAM TQD-G1).

Signal processing methodology—the voice was converted by the ETAS, and abstracted the feature value by the Mel spectrogram. Then, the sound signal with extracted feature values was trained by DenseNet to form the classification network. Finally, the classification network was used to classify and identify the real-time sound data.

Supporting Information

Supporting Information is available from the Wiley Online Library or from the author.

Acknowledgements

Y.J., Y.Z., C.N. contributed equally to this work. The authors are grateful for the support received from National Natural Science Foundation of China (Grant No. 22109012), Natural Science Foundation of Beijing Municipality (Grant No. 2212052), and the Fundamental Research Funds for the Central Universities (Grant No. E1E46805). Informed consent was obtained from the volunteers who participated in the experiments.

Conflict of Interest

The authors declare no conflict of interest.

Data Availability Statement

The data that support the findings of this study are available from the corresponding author upon reasonable request.

Keywords

acoustic sensors, machine learning, self-powered sensors, triboelectric nanogenerators, voice recognition

Received: November 11, 2021

Revised: December 27, 2021

Published online:

- [1] W. Gan, C. Chen, H.-T. Kim, Z. Lin, J. Dai, Z. Dong, Z. Zhou, W. Ping, S. He, S. Xiao, M. Yu, L. Hu, *Nat. Commun.* **2019**, *10*, 5084.
- [2] T. Hianik, *Biosensors* **2021**, *11*, 177.
- [3] A. Espinoza, F. Alves, R. Rabelo, G. Da Re, G. Karunasiri, *Sensors* **2020**, *20*, 1245.
- [4] C. Zhao, K. E. Knisely, D. J. Colesa, B. E. Pflugst, Y. Raphael, K. Grosh, *Sci. Rep.* **2019**, *9*, 3711.
- [5] J. Yang, J. Chen, Y. Su, Q. Jing, Z. Li, F. Yi, X. Wen, Z. Wang, Z. L. Wang, *Adv. Mater.* **2015**, *27*, 1316.
- [6] J. H. Han, K. M. Bae, S. K. Hong, H. Park, J. H. Kwak, H. S. Wang, D. J. Joe, J. H. Park, Y. H. Jung, S. Hur, C. D. Yoo, K. J. Lee, *Nano Energy* **2018**, *53*, 658.
- [7] H. S. Wang, S. K. Hong, J. H. Han, Y. H. Jung, H. K. Jeong, T. H. Im, C. K. Jeong, B. Y. Lee, G. Kim, C. D. Yoo, K. J. Lee, *Sci. Adv.* **2021**, *7*, eabe5683.
- [8] M. Zhu, T. He, C. Lee, *Appl. Phys. Rev.* **2020**, *7*, 031305.
- [9] Z. Sun, M. Zhu, C. Lee, *Nanoenergy Adv.* **2021**, *1*, 81.
- [10] T. He, X. Guo, C. Lee, *iScience* **2021**, *24*, 101934.
- [11] G. Chen, Y. Li, M. Bick, J. Chen, *Chem. Rev.* **2020**, *120*, 3668.
- [12] H. S. Lee, J. Chung, G.-T. Hwang, C. K. Jeong, Y. Jung, J.-H. Kwak, H. Kang, M. Byun, W. D. Kim, S. Hur, S.-H. Oh, K. J. Lee, *Adv. Funct. Mater.* **2014**, *24*, 6914.
- [13] J. H. Han, J.-H. Kwak, D. J. Joe, S. K. Hong, H. S. Wang, J. H. Park, S. Hur, K. J. Lee, *Nano Energy* **2018**, *53*, 198.
- [14] Y. Q. Liu, E. L. Li, X. M. Wang, Q. Z. Chen, Y. L. Zhou, Y. Y. Hu, G. X. Chen, H. P. Chen, T. L. Guo, *Nano Energy* **2020**, *78*, 8.
- [15] Y. H. Jung, S. K. Hong, H. S. Wang, J. H. Han, T. X. Pham, H. Park, J. Kim, S. Kang, C. D. Yoo, K. J. Lee, *Adv. Mater.* **2020**, *32*, 1904020.
- [16] Z. L. Wang, *Rep. Prog. Phys.* **2021**, *84*, 096502.
- [17] S. Niu, S. Wang, L. Lin, Y. Liu, Y. S. Zhou, Y. Hu, Z. L. Wang, *Energy Environ. Sci.* **2013**, *6*, 6184.
- [18] J. Shao, T. Jiang, W. Tang, L. Xu, T. W. Kim, C. Wu, X. Chen, B. Chen, T. Xiao, Y. Bai, Z. L. Wang, *Nano Energy* **2018**, *48*, 292.
- [19] Z. Zhao, Y. Dai, D. Liu, L. Zhou, S. Li, Z. L. Wang, J. Wang, *Nat. Commun.* **2020**, *11*, 6186.
- [20] Y. Li, G. Li, P. Zhang, H. Zhang, C. Ren, X. Shi, H. Cai, Y. Zhang, Y. Wang, Z. Guo, H. Li, G. Ding, H. Cai, Z. Yang, C. Zhang, Z. L. Wang, *Adv. Energy Mater.* **2021**, *11*, 2003921.
- [21] Q. Zheng, Q. Tang, Z. L. Wang, Z. Li, *Nat. Rev. Cardiol.* **2021**, *18*, 7.
- [22] J. An, P. Chen, Z. Wang, A. Berbille, H. Pang, Y. Jiang, T. Jiang, Z. L. Wang, *Adv. Mater.* **2021**, *33*, 2101891.
- [23] K. Dong, Y. Hu, J. Yang, S.-W. Kim, W. Hu, Z. L. Wang, *MRS Bull.* **2021**, *46*, 512.
- [24] H. Guo, X. Pu, J. Chen, Y. Meng, M. H. Yeh, G. Liu, Q. Tang, B. Chen, D. Liu, S. Qi, C. Wu, C. Hu, J. Wang, Z. L. Wang, *Sci. Adv.* **2018**, *3*, eaba4294.
- [25] Z. Y. Huo, Y. J. Kim, I. Y. Suh, D. M. Lee, J. H. Lee, Y. Du, S. Wang, H. J. Yoon, S. W. Kim, *Nat. Commun.* **2021**, *12*, 3693.
- [26] X. Peng, K. Dong, C. Ning, R. Cheng, J. Yi, Y. Zhang, F. Sheng, Z. Wu, Z. L. Wang, *Adv. Funct. Mater.* **2021**, *31*, 2103559.
- [27] X. Peng, K. Dong, C. Ye, Y. Jiang, S. Zhai, R. Cheng, D. Liu, X. Gao, J. Wang, Z. L. Wang, *Sci. Adv.* **2020**, *6*, eaba9624.
- [28] K. Dong, X. Peng, Z. L. Wang, *Adv. Mater.* **2020**, *32*, 1902549.
- [29] R. Zhang, C. Dahlström, H. Zou, J. Jonzon, M. Hummelgård, J. Örtengren, N. Blomquist, Y. Yang, H. Andersson, M. Olsen, M. Norgren, H. Olin, Z. L. Wang, *Adv. Mater.* **2020**, *32*, 2002824.
- [30] H. Y. Guo, J. Chen, L. F. Wang, A. C. Wang, Y. F. Li, C. H. An, J. H. He, C. G. Hu, Y. K. S. Hsiao, Z. L. Wang, *Nat. Sustain.* **2021**, *4*, 147.
- [31] R. Cheng, K. Dong, P. Chen, C. Ning, X. Peng, Y. Zhang, D. Liu, Z. L. Wang, *Energy Environ. Sci.* **2021**, *14*, 2460.
- [32] P. Chen, J. An, R. Cheng, S. Shu, A. Berbille, T. Jiang, Z. L. Wang, *Energy Environ. Sci.* **2021**, *14*, 4523.
- [33] C. Zhang, L. He, L. Zhou, O. Yang, W. Yuan, X. Wei, Y. Liu, L. Lu, J. Wang, Z. L. Wang, *Joule* **2021**, *5*, 1613.
- [34] X. Liang, T. Jiang, Y. Feng, P. Lu, J. An, Z. L. Wang, *Adv. Energy Mater.* **2020**, *10*, 2002123.
- [35] Y. Feng, X. Liang, J. An, T. Jiang, Z. L. Wang, *Nano Energy* **2021**, *81*, 105625.
- [36] X. Yin, D. Liu, L. L. Zhou, X. Y. Li, G. Q. Xu, L. Liu, S. X. Li, C. G. Zhang, J. Wang, Z. L. Wang, *Adv. Funct. Mater.* **2020**, *30*, 2002547.
- [37] X. L. Tan, Z. H. Zhou, L. Q. Zhang, X. Wang, Z. W. Lin, R. Y. Yang, J. Yang, *Nano Energy* **2020**, *78*, 10.
- [38] H. F. Zhao, X. Xiao, P. Xu, T. C. Zhao, L. G. Song, X. X. Pan, J. C. Mi, M. Y. Xu, Z. L. Wang, *Adv. Energy Mater.* **2019**, *9*, 10.
- [39] F. Y. Wang, Z. X. Wang, Y. X. Zhou, C. L. Fu, F. Q. Chen, Y. Z. Zhang, H. W. Lu, Y. H. Wu, L. Chen, H. W. Zheng, *Nano Energy* **2020**, *78*, 11.
- [40] A. F. Yu, M. Song, Y. Zhang, Y. Zhang, L. B. Chen, J. Y. Zhai, Z. L. Wang, *Nano Res.* **2015**, *8*, 765.
- [41] X. Xiao, X. Q. Zhang, S. Y. Wang, H. Ouyang, P. F. Chen, L. G. Song, H. C. Yuan, Y. L. Ji, P. H. Wang, Z. Li, M. Y. Xu, Z. L. Wang, *Adv. Energy Mater.* **2019**, *9*, 1902460.
- [42] W. Z. Qiu, Y. G. Feng, N. Luo, S. G. Chen, D. A. Wang, *Nano Energy* **2020**, *70*, 9.
- [43] X. Fan, J. Chen, J. Yang, P. Bai, Z. L. Li, Z. L. Wang, *ACS Nano* **2015**, *9*, 4236.
- [44] J. Yang, J. Chen, Y. Liu, W. Yang, Y. Su, Z. L. Wang, *ACS Nano* **2014**, *8*, 2649.
- [45] H. Guo, X. Pu, J. Chen, Y. Meng, M. H. Yeh, G. Liu, Q. Tang, B. Chen, D. Liu, S. Qi, C. Wu, C. Hu, J. Wang, Z. L. Wang, *Sci. Robot.* **2018**, *3*, eaat2516.
- [46] Z. L. Wang, *Nano Energy* **2020**, *68*, 104272.
- [47] Z. L. Wang, *Mater. Today* **2017**, *20*, 74.